CrossMark

Facile low-temperature co-precipitation method to synthesize hierarchical network-like g-C$_3$N$_4$/SnIn$_4$S$_8$ with superior photocatalytic performance

Fang Deng[1,2], Xiaoying Lu[1,2], Lina Zhao[1,2], Yiting Luo[1,2], Xule Pei[1,2], Xubiao Luo[1,2,*], and Shenglian Luo[1,2,*]

[1] Key Laboratory of Jiangxi Province for Persistent Pollutants Control and Resources Recycle, Nanchang 330063, People's Republic of China

[2] College of Environmental and Chemical Engineering, Nanchang Hangkong University, Nanchang 330063, People's Republic of China

ABSTRACT

Hierarchical network-like graphitic carbon nitride/SnIn$_4$S$_8$ (g-C$_3$N$_4$/SnIn$_4$S$_8$) composites were prepared through a facile low-temperature co-precipitation method. The g-C$_3$N$_4$/SnIn$_4$S$_8$ composite showed enhanced visible-light absorption. The band gap energies of g-C$_3$N$_4$, pure SnIn$_4$S$_8$, and 15 % g-C$_3$N$_4$/SnIn$_4$S$_8$ are 2.58, 1.8, and 1.68 eV, respectively. The photocurrent and photocatalytic activity of the g-C$_3$N$_4$/SnIn$_4$S$_8$ composites firstly increased and then decreased with increasing g-C$_3$N$_4$ content, and it was found that the optimal 15 % g-C$_3$N$_4$/SnIn$_4$S$_8$ exhibited the highest photocurrent intensity and best photocatalytic performance with complete degradation of MO within 80 min under visible-light irradiation, which is much higher than that of pure SnIn$_4$S$_8$. The effect of main reactive species on the MO degradation follows the order of h$^+$ > $^\bullet$O$_2^-$ > $^\bullet$OH, and the possible degradation mechanism was proposed. Moreover, 15 % g-C$_3$N$_4$/SnIn$_4$S$_8$ exhibits excellent reusability and stability without an obvious decrease of photocatalytic activity after four consecutive photocatalytic degradation–regeneration cycles.

Introduction

Water pollution has posed a potential threat to human health by the food chain system, thus it is particularly significant to develop some reliable methods to resolve water pollution problem [1–4]. By far, adsorption, coagulation, biological treatment, chemical oxidation, electrochemical treatment, and heterogeneous photocatalytic oxidation technology have been established for water purification [5–9]. Among the above techniques, TiO$_2$-based heterogeneous photocatalysis has received much attention due to its low cost, strong oxidation ability, nontoxicity, chemical stability, biocompatibility, and simplicity of operation [10–15]. However, TiO$_2$ has a wide band gap (3.2 eV for anatase and 3.0 eV for

Address correspondence to E-mail: luoxubiao@126.com; sllou@hnu.edu.cn

rutile) and can only respond in the ultraviolet (UV) light region, which restrict its practical application in wastewater treatment [16–20]. Therefore, it is imperative and challenging to develop new and efficient visible-light-responsive photocatalysts.

Ternary chalcogenide compounds possess narrow band gap, high stability, and strong visible-light absorption and thus have received tremendous attention in recent years [21–23]. Stannum indium sulfide ($SnIn_4S_8$) is a common ternary chalcogenide semiconductor and exhibits potential application in photocatalysis [24, 25]. However, single $SnIn_4S_8$ semiconductors usually possess a small specific surface area and fast electron–hole recombination, and the photocatalytic activity of silver-based catalysts is diminished during recycling process, which would depress their photocatalytic efficiency and restrict practical application. To solve these problems, integrating $SnIn_4S_8$ with other proper semiconductors or supports is an effective and feasible strategy for high photocatalytic efficiency.

Graphitic carbon nitride ($g-C_3N_4$), a metal-free polymeric semiconductor, has drawn extensive attention due to its nontoxicity, low cost, suitable band position, excellent electrical conductivity, good thermal–chemical stability, excellent optical performance, and strong absorption of visible light, and has been regarded as a promising visible-light-responsive photocatalyst or an excellent support for many photocatalysts [26–30]. Herein, we first presented low-temperature co-precipitation strategy for the fabrication of $g-C_3N_4/SnIn_4S_8$ composites in this study. The physicochemical and electrochemical properties of $g-C_3N_4/SnIn_4S_8$ composites were studied. The effect of $g-C_3N_4$ content on PL intensity, photocurrent intensity, and the photocatalytic activities of $g-C_3N_4/SnIn_4S_8$ composites under visible-light irradiation was also systematically investigated. Moreover, the possible photocatalytic mechanism of $g-C_3N_4/SnIn_4S_8$ was provided.

Experimental

Materials

Tin (IV) chloride pentahydrate ($SnCl_4·5H_2O$) and indium (III) chloride tetrahydrate ($InCl_3·4H_2O$) were purchased from Aladdin Chemistry Co. Ltd. (Shanghai, China). Thioacetamide (TAA) was purchased from China National Medicine Group Chemical Reagent Co., Ltd. (Shanghai, China). Dicyandiamide, urea, *p*-benzoquinone (BQ), isopropanol (IPA), and triethanolamine (TEOA) were purchased from Sinopharm Chemical Reagent Co., Ltd. (Shanghai, China). Ethanol was supplied by Shantou Xilong Chemical Co., Ltd. (Shantou, China). Methyl orange (MO) was obtained from Shanghai Jingxi Chemical Technology Co., Ltd. (Shanghai, China). All the reagents were of analytical grade and used as received without further purification. Water was purified using a Milli-Q water system (Bedford, USA).

Preparation of $g-C_3N_4$

The $g-C_3N_4$ was prepared by pyrolysis of urea and dicyandiamide in air atmosphere. 3.5 g urea and 1.5 g dicyandiamide were firstly milled for 30 min, then transferred in a muffle furnace, and heated to 530 °C for 4 h to complete the reaction [31].

Preparation of $g-C_3N_4/SnIn_4S_8$ composite via a low-temperature co-precipitation approach

0.421 g of $SnCl_4·5H_2O$ (1.2 mmol) and 1.409 g of $InCl_3·4H_2O$ (4.8 mmol) were dissolved in 96 mL of anhydrous ethanol under continuous magnetic stirring, and then 0.9 g TAA (12 mmol) was added to the above solution. Afterwards, a certain amount of $g-C_3N_4$ was added to the solution. The mixture solution was stirred until a transparent solution was formed, then the above solution was transferred to a 150-mL round-bottom flask with a reflux condenser, placed in a thermostatic bath at 70 °C for 3 h under continuous magnetic stirring, and cooled to room temperature naturally. The obtained yellow precipitate was filtered, washed with distilled water and absolute ethanol several times, and finally dried at 80 °C for 12 h. The samples with different $g-C_3N_4$ content were designated as pure $SnIn_4S_8$, 5 % $g-C_3N_4/SnIn_4S_8$, 10 % $g-C_3N_4/SnIn_4S_8$, 15 % $g-C_3N_4/SnIn_4S_8$, 20 % $g-C_3N_4/SnIn_4S_8$, 30 % $g-C_3N_4/SnIn_4S_8$, and 40 % $g-C_3N_4/SnIn_4S_8$.

Characterization

X-ray diffraction (XRD) patterns of samples were obtained using a Rigaku D/max 2200 PC automatic

X-ray diffractometer (Rigaku, Japan). Transmission electron microscopy (TEM, Hitachi, Japan) and scanning electron microscopy (SEM, Shimadzu, Japan) were used to observe the morphology of the samples. Energy-dispersive spectrometry (EDS, Shimadzu, Japan) was used to confirm the existence of $SnIn_4S_8$ and $g-C_3N_4$. The specific surface area and pore structures of samples were determined using a GEMINI VII 2390 surface area and porosity analyzer (Micromeritics, USA). The reflectance spectra were obtained using a UV-2550 scan UV–Vis spectrophotometer (Shimadzu, Japan) equipped with a Labsphere diffuse reflectance accessory. The photoluminescence (PL) emission spectra were obtained using F-7000 fluorescence spectrophotometer (Hitachi, Japan).

Photocatalytic activity measurement

The photocatalytic activities were evaluated by decomposing MO under visible-light irradiation. A 300 W Xe lamp with a 400 nm cut-off filter was used as the visible-light source. For the typical photocatalytic experiments, 30 mg of photocatalyst was added into 160 mL of 10 mg/L MO solution. Before irradiation, the suspensions were magnetically stirred in the dark for 40 min to reach adsorption–desorption equilibrium. In the dark reaction, 4 mL suspension was sampled at different time intervals and centrifuged immediately to remove suspended photocatalyst powders. The concentration of MO was analyzed using a UV–Vis spectrophotometer at 463 nm.

Regeneration and reuse of spent $g-C_3N_4/$ $SnIn_4S_8$ composite photocatalyst

The spent $g-C_3N_4/SnIn_4S_8$ catalysts were recovered from the mixture solution by centrifugation, regenerated by washing with water and ethanol, and then dried at 80 °C for 4 h. The regenerated $g-C_3N_4/SnIn_4S_8$ catalysts were reused for MO degradation under similar reaction conditions as with the fresh catalysts.

Results and discussion

XRD analysis

The crystal structure of $g-C_3N_4$, pure $SnIn_4S_8$, and 15 % $g-C_3N_4/SnIn_4S_8$ composite was characterized
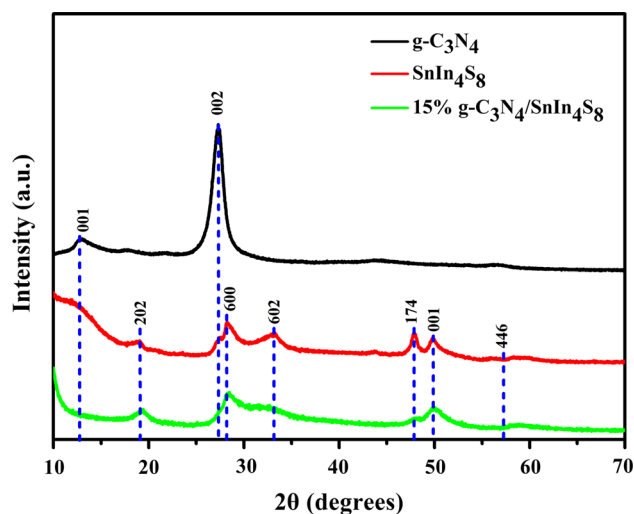
Figure 1 XRD patterns of $g-C_3N_4$, pure $SnIn_4S_8$, and 15 % $g-C_3N_4/SnIn_4S_8$.

by XRD (Fig. 1). Pure $SnIn_4S_8$ and 15 % $g-C_3N_4/$ $SnIn_4S_8$ have similar XRD patterns. The main diffraction peaks at about $2\theta = 28.6°$ and $50.4°$ are observed, which can be indexed to the (600) and (001) crystalline planes of tetragonal phase of $SnIn_4S_8$, respectively. Moreover, it is interesting to note that no $g-C_3N_4$ diffractions are found in the XRD pattern of $g-C_3N_4/SnIn_4S_8$ composite, possibly due to the low loading content of $g-C_3N_4$ or the highly dispersed $g-C_3N_4$ on $SnIn_4S_8$.

Morphology analysis of pure $SnIn_4S_8$ and $g-C_3N_4/SnIn_4S_8$

The morphologies of pure $SnIn_4S_8$ and 15 % $g-C_3N_4/$ $SnIn_4S_8$ are shown in Fig. 2. Pure $SnIn_4S_8$ is composed of a large amount of 3D hierarchical network-like spheres with a diameter ranging from 1 to 2 μm. An enlarged view of an individual $SnIn_4S_8$ sphere shows that the network-like superstructure of pure $SnIn_4S_8$ is constructed by numerous bending two-dimensional nanosheets with a thickness of about 20 nm. In case of 15 % $g-C_3N_4/SnIn_4S_8$, the thickness of nanosheets becomes obviously thinner, and hierarchical pores between nanosheets become obviously larger compared with pure $SnIn_4S_8$. The thinner nanosheets and larger hierarchical pores are beneficial for the multiple scattering of light and light-harvesting capacity, thus it is expected that this structure would improve the photocatalytic activity of $g-C_3N_4/SnIn_4S_8$.

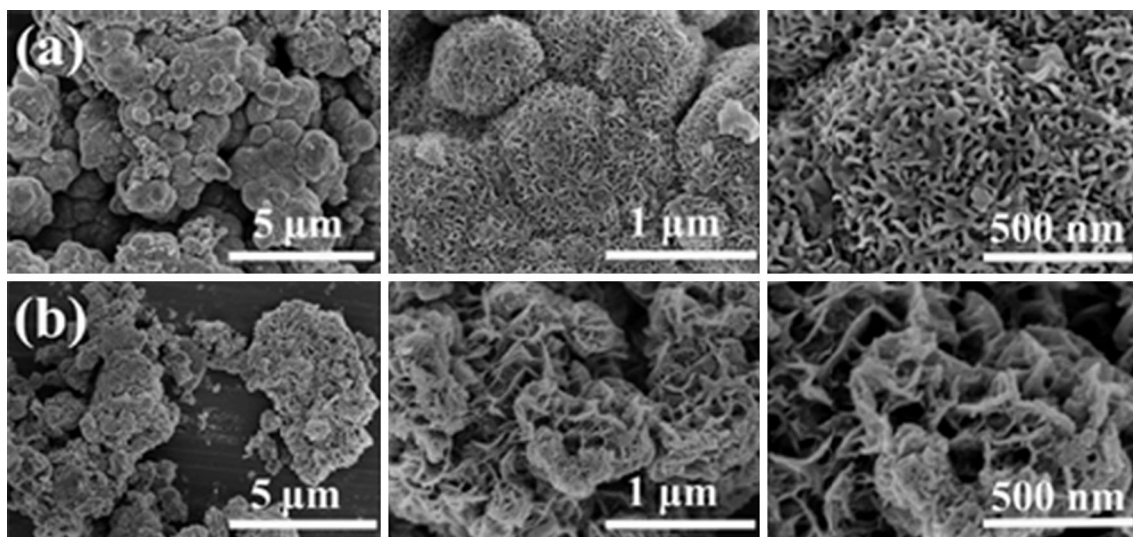Figure 2 SEM images of a pure $SnIn_4S_8$ and b 15 % g-C_3N_4/$SnIn_4S_8$ with different magnifications.
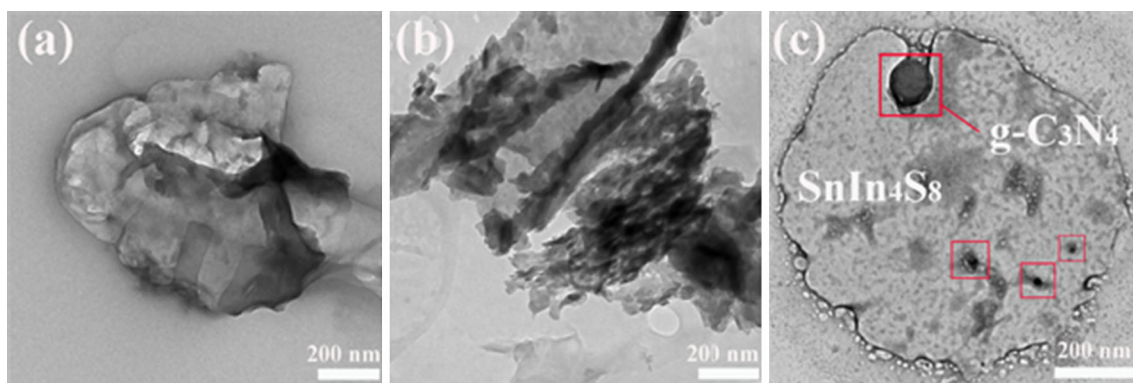
Figure 3 TEM images of a pure $SnIn_4S_8$, b g-C_3N_4, and c 15 % g-C_3N_4/$SnIn_4S_8$.

The microstructure of g-C_3N_4, pure $SnIn_4S_8$, and 15 % g-C_3N_4/$SnIn_4S_8$ composites was further studied by TEM (Fig. 3). The TEM images further confirmed the network-like structure of pure $SnIn_4S_8$, and g-C_3N_4 possessed a loose structure and nanopores with size in the range of 20–50 nm, and it is clear that g-C_3N_4 was successfully dispersed on $SnIn_4S_8$.

EDS analysis

The EDS analysis was used to analyze the chemical composition of pure $SnIn_4S_8$ and 15 % g-C_3N_4/$SnIn_4S_8$ (Fig. 4). It can be seen from Fig. 4 that pure $SnIn_4S_8$ is composed of Sn, In, and S elements. In case of 15 % g-C_3N_4/$SnIn_4S_8$, Sn, In, S, C, and N elements

were observed, confirming the formation of g-C_3N_4/$SnIn_4S_8$ composites.

Specific surface areas and porous structures

The nitrogen adsorption–desorption isotherm and the pore size distribution curves of pure $SnIn_4S_8$ and 15 % g-C_3N_4/$SnIn_4S_8$ composite are shown in Fig. 5. The isotherms of pure $SnIn_4S_8$ and 15 % g-C_3N_4/$SnIn_4S_8$ are classified as type IV according to the Brunauer–Deming–Deming–Teller (BDDT) classification, implying the presence of mesopores (2–50 nm). The shape of the hysteresis loop is of type H3, which is associated with aggregates of plate-like particles, giving rise to slit-like pores. Pure $SnIn_4S_8$

Figure 4 EDS patterns of **a** pure $SnIn_4S_8$ and **b** 15 % g-C_3N_4/$SnIn_4S_8$ composites.

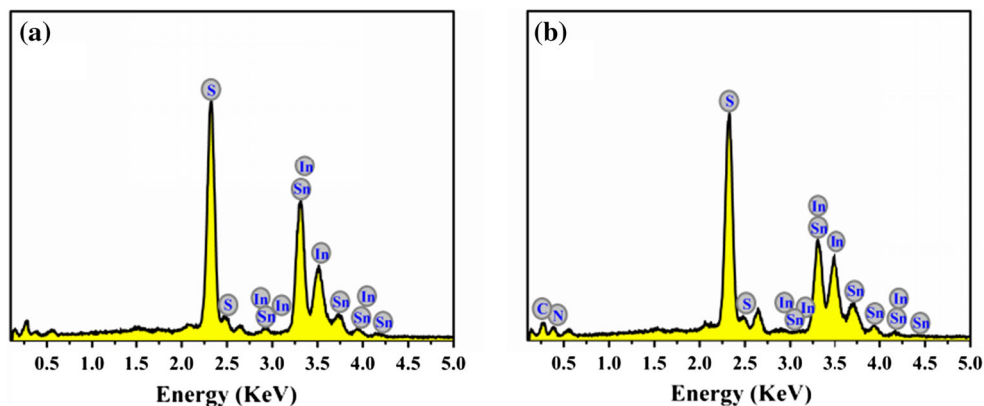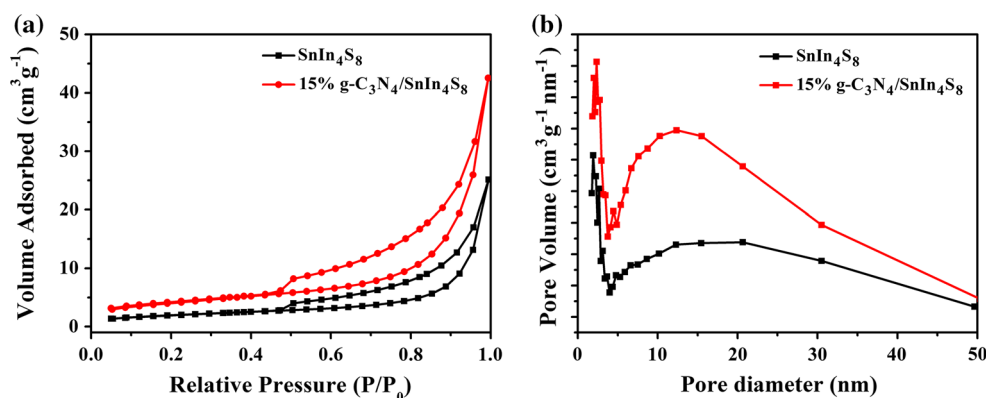**Figure 5 a** Nitrogen adsorption–desorption isotherms and **b** pore size distribution curves of pure $SnIn_4S_8$ and 15 % g-C_3N_4/$SnIn_4S_8$.

and 15 % g-C_3N_4/$SnIn_4S_8$ composites possessed broad and bimodal pore size distribution with small mesopores (2–3 nm) and larger ones (5–30 nm). The BET surface areas of pure $SnIn_4S_8$ and 15 % g-C_3N_4/$SnIn_4S_8$ composites are 14.49 and 21.33 m^2 g^{-1}, respectively. A larger surface area of 15 % g-C_3N_4/$SnIn_4S_8$ provides more surface active sites for the adsorption of the reactive molecules, which is beneficial for the photocatalytic degradation of organic pollutants.

Optical properties

The UV–Vis diffuse reflectance spectra of pure $SnIn_4S_8$, g-C_3N_4, and 15 % g-C_3N_4/$SnIn_4S_8$ composite are shown in Fig. 6a. We can see that the absorption edges of 15 % g-C_3N_4/$SnIn_4S_8$ composite shift significantly to longer wavelength, and the absorption intensity of 15 % g-C_3N_4/$SnIn_4S_8$ composite is stronger than that of pure $SnIn_4S_8$.

The band gap energies of pure $SnIn_4S_8$, g-C_3N_4, and 15 % g-C_3N_4/$SnIn_4S_8$ composite can be estimated from the following equation: $(\alpha h v)^n = k(h v - Eg)$, where α is the absorption coefficient, k is a constant, hv is the

photonic energy, Eg is the absorption band gap energy, and the value of n is 2 and 1/2 for a direct and an indirect band gap semiconductor, respectively. Plots of $(\alpha h v)^2$ versus hv of the samples are shown in Fig. 6b, and the band gap energies of pure $SnIn_4S_8$, 15 % g-C_3N_4/$SnIn_4S_8$, and g-C_3N_4 are estimated to be about 1.8, 1.68, and 2.58 eV, respectively.

PL emission spectra

The separation efficiency of photogenerated electrons and holes can be investigated by PL emission spectra. Figure 7 represents the PL spectra of pure $SnIn_4S_8$ and g-C_3N_4/$SnIn_4S_8$ composites with different g-C_3N_4 content. Pure $SnIn_4S_8$ shows the highest PL intensity, indicating that pure $SnIn_4S_8$ exhibits the highest recombination of electrons and holes and the lowest separation efficiency under visible-light irradiation. Moreover, the PL emission intensity of g-C_3N_4/$SnIn_4S_8$ composites is obviously influenced by the content of g-C_3N_4. With increasing the g-C_3N_4 content from 0 to 15 %, the emission intensity of g-C_3N_4/$SnIn_4S_8$ composite decreased, but further increasing the g-C_3N_4 content results in a dramatic

Figure 6 **a** UV–Vis diffuse reflectance spectra and **b** plots of $(\alpha h v)^2$ versus hv of pure $SnIn_4S_8$, g-C_3N_4, and 15 % g-C_3N_4/$SnIn_4S_8$.
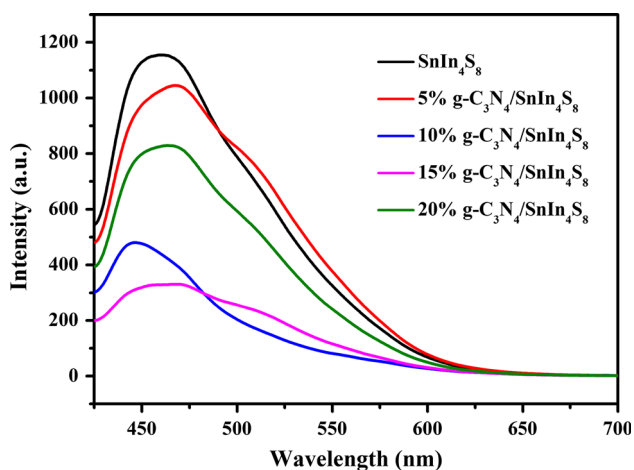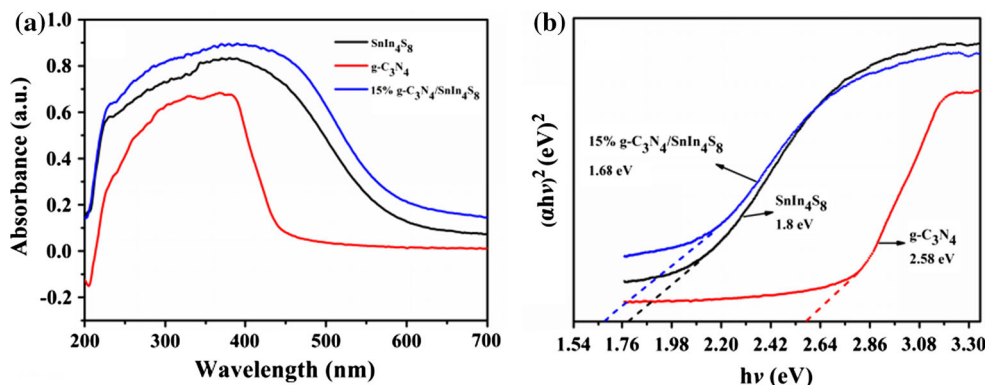

Figure 7 PL spectra of pure $SnIn_4S_8$ and g-C_3N_4/$SnIn_4S_8$ composites with different g-C_3N_4 content.

Figure 8 Transient photocurrent response for g-C_3N_4, pure $SnIn_4S_8$, and g-C_3N_4/$SnIn_4S_8$ composites with different g-C_3N_4 content.

increase of PL emission intensity, leading to the lowest PL emission intensity for 15 % g-C_3N_4/$SnIn_4S_8$ composite. Therefore, it is implied that 15 % g-C_3N_4/$SnIn_4S_8$ composite could exhibit the highest separation efficiency of electron–hole pairs under visible-light irradiation.

Photocurrent analysis

To further confirm the separation efficiency of photogenerated electrons and holes, the transient photocurrent response versus time curves of g-C_3N_4, $SnIn_4S_8$, and g-C_3N_4/$SnIn_4S_8$ composite ITO electrodes under visible-light irradiation were measured (Fig. 8). The photocurrent intensity increased in the order of g-C_3N_4 < pure $SnIn_4S_8$ < 5 % g-C_3N_4/$SnIn_4S_8$ < 10 % g-C_3N_4/$SnIn_4S_8$ < 20 % g-C_3N_4/$SnIn_4S_8$ < 15 % g-C_3N_4/$SnIn_4S_8$, indicating that

g-C_3N_4 content in the composite has an obvious effect on the photocurrent intensity of g-C_3N_4/$SnIn_4S_8$ composite. The photocurrent intensity of g-C_3N_4/$SnIn_4S_8$ composite increased with increasing the g-C_3N_4 content from 0 to 15 %, but decreased with further increasing the g-C_3N_4 content from 15 % to 20 %, leading to the highest photocurrent intensity for 15 % g-C_3N_4/$SnIn_4S_8$ composite. The highest photocurrent intensity of 15 % g-C_3N_4/$SnIn_4S_8$ composite further confirmed its highest separation efficiency of electron–hole pairs under visible-light irradiation, which is consistent with PL results.

Photocatalytic activity

Figure 9 shows the adsorption process in the dark and photocatalytic degradation of MO over pure $SnIn_4S_8$, g-C_3N_4, and g-C_3N_4/$SnIn_4S_8$ composites
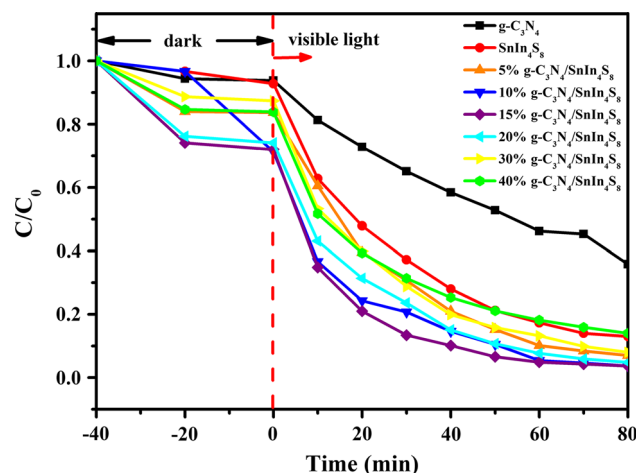
Figure 9 Temporal changes of MO concentration in the presence of pure $SnIn_4S_8$ and $g\text{-}C_3N_4/SnIn_4S_8$ composites with different $g\text{-}C_3N_4$ content.

Figure 10 Effect of different scavengers on the MO photodegradation by 15 % $g\text{-}C_3N_4/SnIn_4S_8$.

under visible-light irradiation. The photocatalytic activity of $g\text{-}C_3N_4/SnIn_4S_8$ composite is higher than that of pure $SnIn_4S_8$ and $g\text{-}C_3N_4$ and is greatly influenced by the $g\text{-}C_3N_4$ content. The photocatalytic activity of $g\text{-}C_3N_4/SnIn_4S_8$ composite is enhanced with increasing the $g\text{-}C_3N_4$ content from 5 % to 15 %. When the content of $g\text{-}C_3N_4$ reaches 15 %, it exhibits the highest photocatalytic activity, giving rise to the almost complete degradation of MO, which is much higher than that of pure $SnIn_4S_8$. However, as the proportion of $g\text{-}C_3N_4$ further increases from 15 to 40 %, the photocatalytic activity decreases gradually though it remains higher than that of pure $SnIn_4S_8$. Possible reason is that appropriate amount of $g\text{-}C_3N_4$ is beneficial for the generation and transfer of photogenerated electrons and holes, while excessive $g\text{-}C_3N_4$ could shield $SnIn_4S_8$ from light as well as promote electron–hole recombination. Therefore, due to the demands of both the charge transfer and light harvesting, the photocatalytic activity of $g\text{-}C_3N_4/SnIn_4S_8$ firstly increases and then decreases with increasing $g\text{-}C_3N_4$ content, which results in the best photocatalytic activity of 15 % $g\text{-}C_3N_4/SnIn_4S_8$.

Photocatalytic mechanism

In order to detect the main reactive species (such as h^+, $^\bullet OH$, and $^\bullet O_2^-$ radicals) of 15 % $g\text{-}C_3N_4/SnIn_4S_8$ composite during photocatalytic process under visible-light irradiation, the trapping experiment of h^+, $^\bullet OH$, and $^\bullet O_2^-$ radicals was investigated by adding
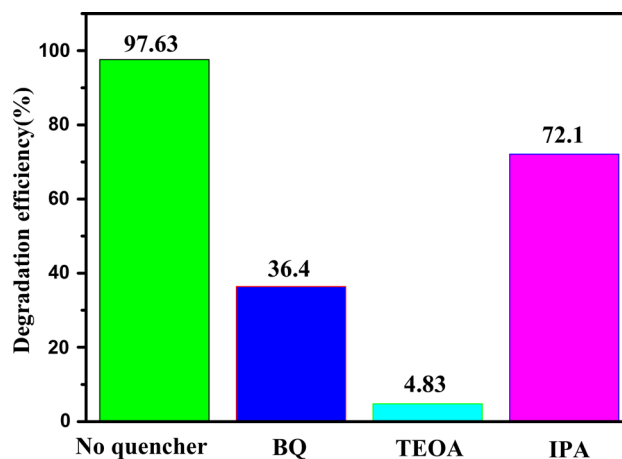
1.0 mmol/L TEOA (a quencher of h^+), 1.0 mmol/L BQ (a quencher of $^\bullet O_2^-$), and 1.0 mmol/L IPA (a quencher of $^\bullet OH$), respectively. As shown in Fig. 10, the degradation efficiency of MO is 97.63 % in the absence of quenchers. When TEOA, BQ, and IPA scavengers were added, the MO degradation efficiency was reduced to 4.83, 36.4, and 72.1 %, respectively. The results indicated that the main reactive species which play crucial roles in the degradation of MO follow the order of $h^+ > {}^\bullet O_2^- > {}^\bullet OH$.

According to the band gap energy and Mott–Schottky plot of $SnIn_4S_8$ (Fig. 11), the conduction band potential (E_{CB}) and valence band potential (E_{VB}) of $SnIn_4S_8$ can be calculated. The flat-band potential (E_{fb}) of $SnIn_4S_8$ can be estimated from the Mott–Schottky equation:

$$\frac{1}{C^2} = \frac{2}{\varepsilon\varepsilon_o N_d}\left(E - E_{fb} - \frac{k_B T}{e}\right),$$

where C is the space charge capacitance, ε is the dielectric constant of the semiconductor, ε_0 is the permittivity of free space, N_d is the donor density, E is the applied potential, E_{fb} is the flat-band potential, kB is Boltzmann's constant (1.38×10^{-23} J K^{-1}), T is the absolute temperature, and e is the electronic charge. The E_{fb} value can be determined by extrapolating the linear part of the curve to $\frac{1}{C^2} = 0$, and the E_{fb} value of $SnIn_4S_8$ is about -0.45 V versus the saturated calomel electrode (SCE), and is about -0.21 V versus NHE. Supposing the difference between flat-
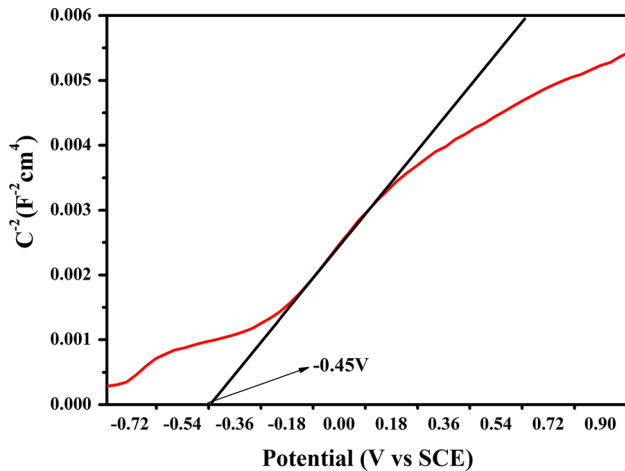
Figure 11 Mott–Schottky plots for $SnIn_4S_8$.

electrons (e^-) and holes (h^+) can be excited from the valence band (VB) and conduction band (CB) of g-C_3N_4 and then transferred to the VB and CB of $SnIn_4S_8$, respectively. The accumulated e^- on the surface of $SnIn_4S_8$ can react with adsorbed O_2 to form superoxide radicals ($^\bullet O_2^-$). A majority of $^\bullet O_2^-$ radicals play important roles in the MO degradation, and the rest of $^\bullet O_2^-$ could further react with H_2O to generate hydroxyl radicals ($^\bullet OH$), which also have some impact on the degradation of MO. The h^+ in the VB of $SnIn_4S_8$ can preferentially attack MO adsorbed onto the surface of g-C_3N_4/$SnIn_4S_8$ composites, and then MO can be transformed to degradation products.

Regeneration and reuse of spent g-C_3N_4/$SnIn_4S_8$ composite

To test the stability and reusability of 15 % g-C_3N_4/$SnIn_4S_8$, the 15 % g-C_3N_4/$SnIn_4S_8$ composite was reused four times for photocatalytic reaction under the same conditions, and the results are shown in Fig. 13a. There is no obvious decrease in the photocatalytic activity of the 15 % g-C_3N_4/$SnIn_4S_8$ after four consecutive photocatalytic degradation cycles, indicating that the 15 % g-C_3N_4/$SnIn_4S_8$ is stable and can be used repeatedly. Moreover, the structure of the regenerated 15 % g-C_3N_4/$SnIn_4S_8$ after four consecutive cycles was characterized by XRD, and the results are shown in Fig. 13b. It can be seen that

band potential and conduction band potential can be negligible for n-type semiconductors [32], the E_{CB} value (-0.21 V vs NHE) is approximately equal to the E_{fb} value. The E_{VB} of $SnIn_4S_8$ can be calculated by empirical equation ($E_{VB} = E_{CB} + E_g$), and the E_{VB} value of $SnIn_4S_8$ is about 1.59 V versus NHE.

Based on the trapping experiment results, E_{CB} and E_{VB} values of $SnIn_4S_8$, and the reported literatures, the generation and transfer of the photogenerated holes and electrons in g-C_3N_4/$SnIn_4S_8$ composites are illustrated in Fig. 12. As shown in Fig. 12, under visible-light illumination, the photogenerated

Figure 12 Photocatalytic mechanism of g-C_3N_4/$SnIn_4S_8$ composite under visible-light irradiation.
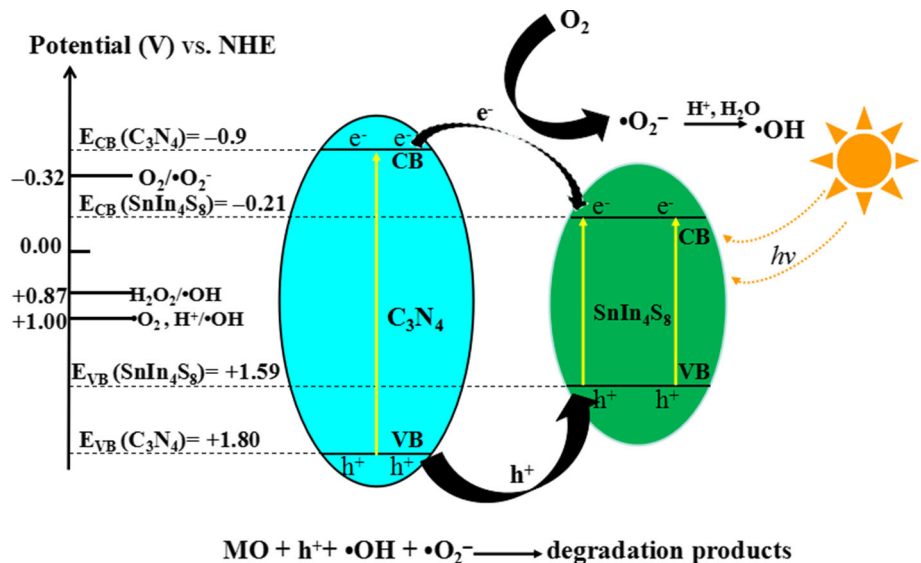
Figure 13 **a** Regeneration and reuse of 15 % g-C_3N_4/SnIn$_4S_8$ and **b** XRD patterns of the regenerated 15 % g-C_3N_4/SnIn$_4S_8$ after four consecutive cycles.
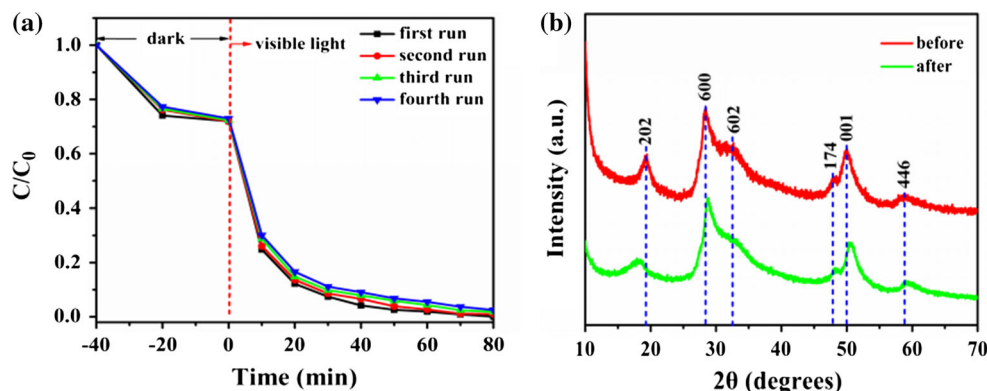
there is no significant change of crystal structure, and the main diffraction peaks of the regenerated 15 % g-C_3N_4/SnIn$_4S_8$ are approximately consistent with those of the fresh counterpart.

Conclusions

We first successfully prepared hierarchical network-like g-C_3N_4/SnIn$_4S_8$ composites with visible-light response and high photocatalytic activity by low-temperature co-precipitation method. The band gap energies of g-C_3N_4, pure SnIn$_4S_8$, and 15 % g-C_3N_4/SnIn$_4S_8$ are 2.58, 1.8, and 1.68 eV, respectively. The g-C_3N_4 content in g-C_3N_4/SnIn$_4S_8$ composites was optimized, and the optimal 15 % g-C_3N_4/SnIn$_4S_8$ composites showed the maximum photocurrent intensity and the best photocatalytic performance with complete degradation of MO within 80 min under visible-light irradiation, which is much higher than that of pure SnIn$_4S_8$. The main reactive species which affect MO degradation efficiency follow the order of $h^+ > {}^{\bullet}O_2^- > {}^{\bullet}OH$, and the possible degradation mechanism was proposed. Moreover, 15 % g-C_3N_4/SnIn$_4S_8$ exhibits excellent reusability and stability without an obvious decrease of photocatalytic activity after four consecutive photocatalytic degradation cycles.

Acknowledgements

References

[1] Schwarzenbach RP, Egli T, Hofstetter TB, Gunten U, Wehrli B (2010) Global water pollution and human health. Annu Rev Environ Resour 35:109–136

[2] Azizullaha A, Khattakb MNK, Richtera P, Hädera DP (2011) Water pollution in Pakistan and its impact on public health—a review. Environ Int 37:479–497

[3] Lu YL, Song S, Wang RS, Liu ZY, Meng J, Sweetman AJ, Jenkins A, Ferrier RC, Li H, Luo W, Wang TY (2015) Impacts of soil and water pollution on food safety and health risks in China. Environ Int 77:5–15

[4] Huang YQ, Wong CKC, Zheng JS, Bouwman H, Barra R, Wahlström B, Neretin L, Wong MH (2012) Bisphenol A (BPA) in China: a review of sources, environmental levels, and potential human health impacts. Environ Int 42:91–99

[5] Cheng Z, Liao J, He B, Zhang F, Zhang F, Huang X, Zhou L (2015) Porous Ag/polymer composite microspheres for adsorption and catalytic degradation of organic dyes in aqueous solutions. ACS Sustain Chem Eng 3:1677–1685

[6] Zhang Q, Liu S, Zhang Y, Zhu A, Li J, Du X (2016) Enhancement of the photocatalytic activity of g-C_3N_4 via treatment in dilute NaOH aqueous solution. Mater Lett 171:79–82

[7] Zhang Y, Zhang Q, Shi Q, Cai Z, Yang Z (2015) Acid-treated g-C_3N_4 with improved photocatalytic performance in the reduction of aqueous Cr(VI) under visible-light. Sep Purif Technol 142:251–257

[8] Mondal T, Bhowmick AK (2013) Synthesis and characterization of bi-functionalized graphene and expanded graphite using *n*-butyl lithium and their use for efficient water soluble dye adsorption. J Mater Chem A 1:8144–8153

[9] Yang Y, Liao H, Tong Z, Wang CY (2015) Porous Ag/polymer composite microspheres for adsorption and catalytic degradation of organic dyes in aqueous solutions. Compos Sci Technol 107:137–144

[10] Deng F, Liu Y, Luo XB, Wu SL, Luo SL, Au CT, Qi RX (2014) Sol-hydrothermal synthesis of inorganic-framework

molecularly imprinted TiO$_2$/SiO$_2$ nanocomposite and its preferential photocatalytic degradation towards target contaminant. J Hazard Mater 278:108–115

[11] Wei HT, Zhang Q, Zhang YC, Yang ZJ, Zhu AP, Dionysiou DD (2015) Enhancement of the Cr(VI) adsorption and photocatalytic reduction activity of g-C3N4 by hydrothermal treatment in HNO3 aqueous solution. Appl Catal A (2015)

[12] Li K, Gao SM, Wang QY, Xu H, Wang ZY, Huang BB, Dai Y, Lu J (2015) In-situ-reduced synthesis of Ti^{3+} self-doped TiO$_2$/g-C$_3$N$_4$ heterojunctions with high photocatalytic performance under LED light irradiation. ACS Appl Mater Interf 7:9023–9030

[13] Calvo ME, Colodrero S, Rojas TC, Anta JA, Ocana M, Míguez H (2008) Photoconducting Bragg mirrors based on TiO$_2$ nanoparticle multilayers. Adv Funct Mater 18:2708–2715

[14] Lv K, Yu J, Cui L, Chen S, Li M (2011) Preparation of thermally stable anatase TiO$_2$ photocatalyst from TiOF$_2$ precursor and its photocatalytic activity. J Alloys Compd 509:4557–4562

[15] Deng F, Min LJ, Luo XB, Wu SL, Luo SL (2013) Visible-light photocatalytic degradation performances and thermal stability due to the synergetic effect of TiO$_2$ with conductive copolymers of polyaniline and polypyrrole. Nanoscale 5:8703–8710

[16] Wang TX, Zhang YC, Ding T (2014) One-step solvothermal synthesis of SnIn$_4$S$_8$/TiO$_2$ nanocomposite with enhanced visible-light-activated photocatalytic activity. Mater Lett 123:153–155

[17] Wang J, Tafen DN, Lewis JP, Hong ZL, Manivannan A, Zhi MJ, Li M, Wu NQ (2009) Origin of photocatalytic activity of nitrogen-doped TiO$_2$ nanobelts. J Am Chem Soc 131:12290–12297

[18] Chen CQ, Li P, Wang GZ, Yu Y, Duan FF, Chen CY, Song WG, Qin Y, Knez M (2013) Nanoporous nitrogen-doped titanium dioxide with excellent photocatalytic activity under visible light irradiation produced by molecular layer deposition. Angew Chem Int Ed 52:9196–9200

[19] Zhao ZG, Miyauchi M (2008) Nanoporous-walled tungsten oxide nanotubes as highly active visible-light-driven photocatalysts. Angew Chem Int Ed 47:7051–7055

[20] Chen HM, Chen CK, Chang YC, Tsai CW, Liu RS, Hu SF, Chang WS, Chen KH (2010) Quantum dot monolayer sensitized ZnO nanowire-array photoelectrodes: true efficiency for water splitting. Angew Chem Int Ed 49:5966–5969

[21] Chai B, Peng TY, Zeng P, Zhang XF, Liu XJ (2011) Template-free hydrothermal synthesis of ZnIn$_2$S$_4$ floriated

microsphere as an efficient photocatalyst for H$_2$ production visible-light irradiation. J Phys Chem C 115:6149–6155

[22] Wang L, Li XY, Teng W (2013) Efficient photocatalytic reduction of aqueous Cr(VI) over flower-like SnIn$_4$S$_8$ microspheres under visible light illumination. J Hazard Mater 244–245:681–688

[23] Yan TJ, Li LP, Li GS, Wang YJ, Hu WB, Guan XF (2011) Porous SnIn$_4$S$_8$ microspheres in a new polymorph that promotes dyes degradation under visible light irradiation. J Hazard Mater 186:272–279

[24] Bi Y, Ouyang SX, Cao J, Ye JH (2011) Facile synthesis of rhombic dodecahedral AgX/Ag$_3$PO$_4$ (X = Cl, Br, I) heterocrystals with enhanced photocatalytic properties and stabilities. Phys Chem Chem Phys 13:10071–10075

[25] Thomas A, Fischer A, Goettmann F, Antonietti M, Muller JO, Schlogl R, Carlsson JM (2008) Graphitic carbon nitride materials: variation of structure and morphology and their use as metal-free catalysts. J Mater Chem 18:4893–4908

[26] Li TT, Zhao LH, He YM, Cai J, Luo MF, Lin JJ (2013) Synthesis of g-C$_3$N$_4$/SmVO$_4$ composite photocatalyst with improved visible light photocatalytic activities in RhB degradation. Appl Catal B: Environ 129:255–263

[27] Xue JJ, Ma SS, Zhou YM, Zhang ZW, He M (2015) Facile photochemical synthesis of Au/Pt/g-C$_3$N$_4$ with plasmon-enhanced photocatalytic activity for antibiotic degradation. ACS Appl Mater Interf 7:9630–9637

[28] Xu H, Yan J, Xu YG, Song YH, Li HM, Xia JX, Huang CJ, Wan HL (2013) Novel visible-light-driven AgX/graphite-like C$_3$N$_4$ (X = Br, I) hybrid materials with synergistic photocatalytic activity. Appl Catal B: Environ 129:182–193

[29] Wang XC, Chen XF, Thomas A, Fu XZ, Antonietti M (2009) Metal-containing carbon nitride compounds: a new functional organic-metal hybrid. Mater Adv Mater 21:1609–1612

[30] Ge L, Zuo F, Liu JK, Ma Q, Wang C, Sun DZ, Bartels L, Feng PY (2012) Synthesis and efficient visible light photocatalytic hydrogen evolution of polymeric g-C$_3$N$_4$ coupled with CdS quantum dots. J Phys Chem C 116:13708–13714

[31] Zhang M, Xu J, Zong RL, Zhu YF (2014) Enhancement of visible light photocatalytic activities via porous structure of g-C$_3$N$_4$. Appl Catal B: Environ 147:229–235

[32] Lim J, Murugan P, Lakshminarasimhan N, Kim JY, Lee JS, Lee S, Choi W (2014) Synergic photocatalytic effects of nitrogen and niobium co-doping in TiO$_2$ for the redox conversion of aquatic pollutants under visible light. J Catal 310:91–99